Effect of the alkyl linker length on the photoisomerization of hydrazone switches on metal surfaces

Author(s):
Zheng, Liqing; Yang, Sirun; Krähenbühl, Sven; Rybkin, Vladimir V.; Lan, Jinggang; Aprahamian, Ivan; Zenobi, Renato

Publication date:
2022-06

Permanent link:
https://doi.org/10.3929/ethz-b-000531705

Originally published in:
Materials Today Chemistry 24, https://doi.org/10.1016/j.mtchem.2022.100797

Funding acknowledgement:
741431 - Nanoscale Vibrational Spectroscopy of Sensitive 2D Molecular Materials (EC)

Materials Today Chemistry 24 (2022) 100797

Contents lists available at ScienceDirect

Materials Today Chemistry

journal homepage: www.journals.elsevier.com/materials-today-chemistry/

Effect of the alkyl linker length on the photoisomerization of hydrazone switches on metal surfaces

L.-Q. Zheng [a, d], S. Yang [b, d], S. Krähenbühl [a], V.V. Rybkin [c], J. Lan [c, **], I. Aprahamian [b, ***], R. Zenobi [a, *]

[a] Department of Chemistry and Applied Biosciences, ETH Zurich, Vladimir-Prelog-Weg 3, CH 8093, Switzerland
[b] Department of Chemistry, Dartmouth College, Hanover, NH, 03755, United States
[c] Department of Chemistry, University of Zurich, Winterthurerstrasse 190, CH 8057, Switzerland

ARTICLE INFO

Article history:
Received 21 November 2021
Received in revised form
15 January 2022
Accepted 18 January 2022
Available online xxx

Keywords:
Organic photoswitches
Raman spectroscopy
Surface quenching
Photocontrollable surface

ABSTRACT

A series of bistable hydrazone switches containing alkyl thiolate linkers of various lengths (C*n* HAT, n = 3, 8, 10, and 11) were synthesized. We explore the length effect of the carbon chain on the photoisomerization of hydrazone switches using UV–vis spectroscopy and tip-enhanced Raman spectroscopy (TERS). The conversion efficiency (photostationary state, PSS, after irradiation at 415 or 340 nm) of the isomerization of C*n* HAT monolayers on Au rises with the increasing length of the alkyl chain, with an optimum result for *n*-octyl (C8) thiolate or longer linkers. The low PSS_{415} of C3 HAT is attributed to strong quenching by the metal surface, as confirmed by density functional theory (DFT) calculations based on a one-dimensional double-well model. The partial trap of photo-induced hot carriers in the excited states of C3 HAT in the potential well of Au reduces the lifetime of its excited states. Such calculation results provide insight into the detailed mechanism of the surface quenching effect. Furthermore, UV–vis results suggest that after irradiation at 415 nm, C*n* HATs cannot isomerize when bound to Ag; higher photon energies are necessary in this case. These results validate the previously proposed substrate-mediated isomerization mechanism.

1. Introduction

Molecular photoswitches [1,2], molecules that undergo structural changes upon optical stimuli, enable scientists to remotely control the motion of molecules and to modulate their properties and functions. These compounds attract considerable attention, as they play significant roles in various fields ranging from nanotechnology to biology [3–7], and their great potential has been shown in applications such as data storage [8,9], drug delivery [4,7,10], sensing [11,12], catalysis [13], and energy conversion [14], etc. Over the past decades, various types of photoswitches have been developed and explored, including azobenzenes [15], diarylethenes [16], spiropyrans [17], and hydrazones [11]. Among these photochromic compounds, hydrazone-based switches [18], which are a new addition to the molecular toolbox available to the community, uniquely combine ease of synthesis, bistability (thermal half-life as long as 5,300 years [19]), fatigue resistance, multiphase switchability in an easily accessible and modular structural framework [20,21]. Our recent systematic structure-property study using a family of hydrazone switches has shown that their properties, including activation wavelengths, photostationary states (PSSs), quantum yield, thermal half-lives, and solution/solid-state fluorescence characteristics, are highly dependent on the electronic property of the substituent groups of the hydrazone [22]. Optimization of these properties will pave avenues to opportunities for developing new applications, and thus, greatly enhance the proliferation of hydrazone switches as effective tools in various research fields.

When it comes to the development of the applications of photoswitches, one is faced with the challenge of engineering these molecular switches onto adaptive surfaces/materials. Obviously, the photoisomerization of molecular switches also depends on their chemical and physical environments. For instance, an azobenzene derivative, azobenzene thiol, fails to isomerize when lying flat on a gold surface because of a surface quenching effect [23].

* Corresponding author.
** Corresponding author.
*** Corresponding author.
E-mail addresses: jinggang.lan@chem.uzh.ch (J. Lan), ivan.aprahamian@dartmouth.edu (I. Aprahamian), zenobi@org.chem.ethz.ch (R. Zenobi).
[d] Equal contribution.

https://doi.org/10.1016/j.mtchem.2022.100797

Such a quenching effect is expected to be significantly reduced when the distance between the hydrazone and the metal surface increases, as the rate of both energy ($\sim 1/d^4$) [24] and electron ($\sim e^{-d}$) [25] transfer are strongly distance-dependent. To examine the influence of a proximal metal surface on the isomerization efficiency and to minimize the surface quenching effect, and thus, improve the PSS of the photoswitches, we studied the effect of systematically varying the distance between the hydrazone switch and the metal surface. Thus far, questions about the influence of the chemical structure of photoswitches on metal surfaces on their isomerization properties have not been fully answered. Understanding these effects will facilitate the development process of their real-world applications.

When it comes to monolayer analysis, one is faced with the extremely small quantities of material available, which renders many conventional spectroscopic approaches such as NMR inapplicable. Fortunately, there are techniques that are sufficiently sensitive to analyze molecular monolayers, such as scanning probe microscopy (SPM) [26,27], UV–vis spectroscopy [28], and TERS [23,29,30]. SPM provides topographic and electronic structure information of the analyte but very limited chemical information. UV–vis spectroscopy provides useful information from the maximum absorption wavelength of molecules, and TERS gives detailed chemical information if the signals obtained can be assigned with the help of theoretical calculations.

TERS combines SPM with plasmon-enhanced Raman spectroscopy [31–33] and therefore provides chemical fingerprint and topographic information simultaneously. Because of the strong and highly confined field in a plasmonic nanocavity at the tip apex, the spatial resolution of TERS reaches a few nanometers [34–36], and even down to the Å scale (submolecular resolution) under ultrahigh vacuum and cryogenic conditions [37–39]. TERS has been demonstrated to be a powerful analytical technique for the study of molecular switches, including azobenzene-based [23,29] and hydrazone-based [30] switches. Recently, we reported a study of a hydrazone switch functionalized with a C6 alkyl thiolate linker (C6 HAT) anchored on various metal surfaces using TERS and UV–vis spectroscopy [30]. We found that C6 HAT cannot isomerize on an Ag surface when irradiated at 415 nm (the activation wavelength for the *Z*-to-*E* isomerization); higher photon energies were required to cause photoisomerization in this case. Based on this finding and supported by density functional theory (DFT) calculations, we proposed a substrate-mediated photoisomerization mechanism to explain the behavior of C6 HAT on these metal surfaces. This mechanism predicts a significant influence of the length of the alkyl linker on the photoisomerization of hydrazone switches, but this length effect has not been explored experimentally.

Here we study this length effect systematically. We thus synthesized a series of hydrazone thiol (HAT) switches containing an alkyl thiolate linker allowing us to anchor these molecules onto a metal surface. To verify the effect of the distance between the photo-responsive functional group (C=N) and the metal surface on the isomerization of HAT, the number of carbon atoms (Cn) of the alkyl linker was designed to be 3, 8, 10, and 11, as shown in Scheme 1. We investigated the photoisomerization behavior of these hydrazone thiolate switches (C*n* HAT, Fig. 1a) in solution, in the solid state, and when assembled as a monolayer on a metal surface, after irradiating them at $\lambda = 415$ nm or 340 nm. For this, different analytical techniques were employed, including NMR spectroscopy (solution phase), UV–vis spectroscopy (solution phase and at the monolayer level), confocal Raman spectroscopy (solid state), and TERS (at the monolayer level). Finally, TERS mapping was also used to monitor and quantify the photoisomerization of C*n* HAT self-assembled monolayers (SAMs) on Au. The photoisomerization behavior of C*n* HATs was comprehensively studied from various aspects, which shed light on the substrate-mediated photoisomerization mechanism for hydrazone switches on metal surfaces.

2. Materials and methods

2.1. Materials for molecule synthesis

All reagents and starting materials were purchased from commercial vendors and used as supplied unless otherwise indicated. All experiments were conducted under air unless otherwise noted. Compounds were purified by column chromatography using silica gel (SiliCycle®, 60 Å, 230–400 mesh) as stationary phase and solvents mixtures used during chromatography were reported as volume ratios unless otherwise noted. Deuterated solvents were purchased from Cambridge Isotope Laboratories, Inc. and used as received. ^{1}H NMR, ^{13}C NMR, and 2D NMR spectra were recorded on a 500, 600, or 800 MHz NMR spectrometer, with carrier frequencies of 500.13, 600.13, or 799.75 MHz for ^{1}H nuclei, and on 600 or 800 MHz NMR spectrometers with carrier frequencies of 150.9 and 201.1 MHz for ^{13}C nuclei. Chemical shifts are quoted in ppm and were calibrated using the residual solvent peak as the reference. ESI mass spectra were obtained on a Waters Quattro II ESI mass spectrometer. Melting points were measured on an Electrothermal Thermo Scientific IA9100X1 digital melting point instrument.

2.2. Photoisomerization in solution

Irradiation experiments involving photoswitches in toluene were conducted with a stand-alone xenon arc lamp system (Model: LB-LS/30, Sutter Instrument Co.) outfitted with a SMART SHUTTER controller (Model: LB10-B/IQ, Sutter Instrument Co.) and a liquid light guide LLG/250. 340 (part number: 340HC10-25) and 410 (part number: 410FS10-25) nm light filters purchased from Andover Corporation were used in the irradiation experiments. UV–vis spectra were recorded on a Shimadzu UV-1800 UV–vis spectrophotometer.

2.3. Substrate preparation

Template stripped Au substrates [40] were prepared by thermally evaporating 200 nm Au film onto Si (100) wafers. The Si wafers were sonicated in ethanol for 15 min and then immersed in Piranha solution for 30 min. Next, these Si wafers were flushed with large amounts of ultrapure water and dried with N_2 prior to use.

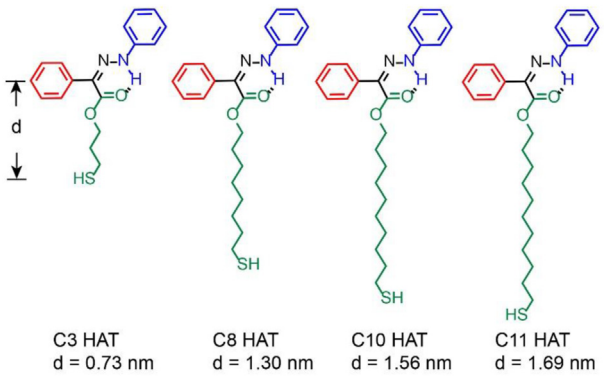

Scheme 1. Molecular structure of the *Z* isomer of synthesized C*n* HAT (n = 3, 8, 10, 11).

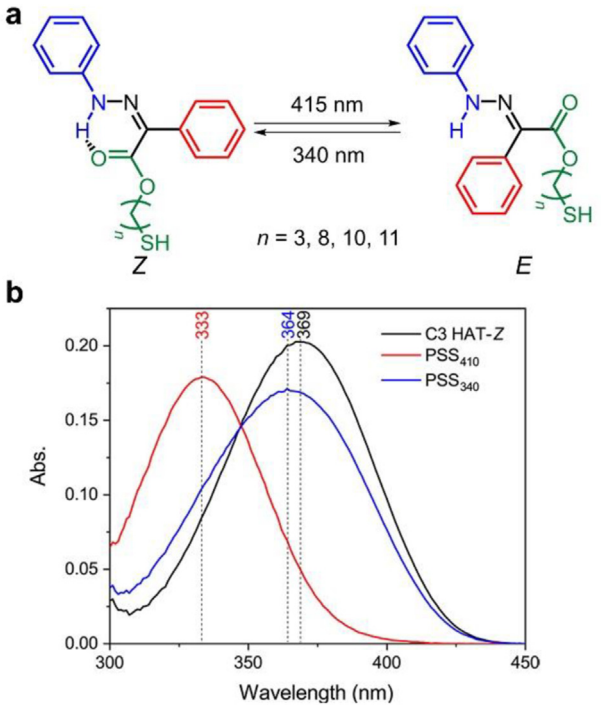

Fig. 1. a. *Z*/*E* photoisomerization of C*n* HAT where n corresponds to the number of carbon atoms in the linker. b. UV–vis spectra of C3 HAT in toluene (1×10^{-5} M) before (black curve) and after irradiation with 410 nm light (red curve), followed by irradiation with 340 nm light (blue curve).

After deposition, pieces of glass (0.5 cm × 2 cm) were glued onto the surface of Au by glue (Thorlabs GmbH, Germany), which can be cured by irradiation with UV light (365 nm) for 20 min. The as-prepared Au substrates were freshly stripped from the Si wafer before use. The root mean squared roughness (RMS) of these Au substrates is around 0.47 nm, based on STM images.

2.4. Cn HAT self-assembled monolayer (SAM) preparation and light irradiation setup

A freshly stripped metal substrate was immersed overnight in 1 mM solution of C6 in ethanol to allow the formation of a SAM on the surface. In the measurement of C3 HAT on Au diluted with hexanethiol, the substrate was immersed in the mixed solution of C3 HAT and hexanethiol ($c_{(C6\ HAT)}$: $c_{(propanethiol)}$ is 1:10) for 2 h. After immersion, the sample was rinsed with ethanol and dried under an N_2 flow. A 1 W UV LED (Xinhuakai Ltd, Shenzhen, China) with a central wavelength of 415 nm and a bandwidth of 25 nm was used as a light source. Another 1W UV LED (Xinhuakai Ltd, Shenzhen, China) with central wavelengths of 340 nm and a bandwidth of 50 nm was also used as a light source. The distance between the light source and the sample was kept at 1 mm. The irradiation time was always 1 min.

2.5. STM-TERS measurements

STM-TERS measurements were performed on a top illumination TERS instrument that combines STM with a Raman spectrometer (NT-MDT, Russia, NTEGRA Spectra Upright). Electrochemically etched Ag tips [41] were used to obtain both the topography and TER spectra. A 632.8 nm He–Ne laser was used as the excitation source. For all measurements, the tunneling current setpoint was 200 pA, the tunneling bias was 0.6 V, and the intensity of the laser was 70 μW with a 1 s exposure time per spectrum.

2.6. UV–vis measurements of Cn HAT SAMs on metal surfaces

UV–vis spectra of C*n* HAT (n = 3, 8, 10, 11) SAMs were recorded by a V660 UV–vis spectrophotometer (Brechbühler AG, Switzerland) and a Genesys 10S UV–vis spectrophotometer (Thermo Scientific, USA). The sample was prepared using the following method: a metal film of Au or Ag with a thickness of 10 nm was prepared on quartz by physical vapor deposition under high vacuum (MED 020, BAL-TEC, Leica microsystems GmbH, Switzerland). The UV–vis spectrum of this metal substrate was collected first, and then it was immersed in an ethanoic C*n* HAT solution for 2 h to obtain the C*n* HAT SAM on the metal substrate. After immersion, the sample was rinsed with ethanol and dried under a flow of N_2. The UV–vis spectrum of the C*n* HAT SAM on the metal substrate was then collected in the absorbance mode. The irradiation of the C*n* HAT SAM was performed *ex situ*.

2.7. Density functional theory (DFT) calculations

DFT calculations were carried out using the CP2K package [42,43]. PBE functional [44] with Grimme D3 correction [45] have been applied to study Cn adsorbed on Au(111) surface. The Kohn-Sham DFT has been solved in the framework of the Gaussian and plane waves method [46,47]. A plane-wave energy cut-off of 500 Ry and DZVP-MOLOPT-SR-GTH basis sets [46] with Goedecker-Teter-Hutter (GTH) pseudopotentials [48,49] were used to describe the surfaces and molecules. The Fermi-Dirac smearing has been employed to study the metallic system, and the electronic temperature was set to 300 K. The Au(111) surface is constructed using a four-layer (6 × 6) slab, which consists of 144 atoms. The geometry optimizations are carried out by keeping the two bottom layers fixed at the initial coordinates to maintain the bulk behavior. The projected density of states is calculated based on the optimized geometries.

3. Results and discussion

3.1. Molecular design and synthesis

The chemical structure of the C*n* HATs is very similar to that of the C6 HAT reported before. An alkyl thiolate linker of various lengths ranging from 0.7 nm to 1.7 nm was attached to the ester moiety of a hydrazone skeleton [50], which has a thermal half-life of 255 years in toluene. The synthetic approach followed a procedure reported in the literature [30], with yields between 51 and 78%. Products were characterized using NMR spectroscopy (Figs. S1-S8) and high-resolution mass spectrometry. The corresponding bromine terminated model compounds (Cn Br) were also synthesized and characterized (Figs. S9-S16).

3.2. Photoisomerization of Cn HATs (n = 3, 8, 10, 11) in toluene

We first employed UV–vis spectroscopy to study the photoisomerization of the synthesized C*n* HAT switches in toluene. The UV–vis spectra of C3 HAT in toluene before and after irradiation at $\lambda = 410$ nm or 340 nm are shown in Fig. 1b, and the UV–vis spectra of C8–C11 HAT in toluene are shown in Fig. S17. The absorption maxima (λ_{max}) of all four *Z*-C*n* HAT in toluene appears at 369 nm. Following irradiation of the C*n* HAT solutions by 410 nm light, λ_{max} of these compounds shifts to 333 nm, indicating the occurrence of *Z*-to-*E* isomerization. Notably, the shift of λ_{max} in the UV–vis spectra of all C*n* HAT solutions is exactly the same as that observed in the UV–vis spectra of C6 HAT in toluene upon irradiation by 410 nm [30]. The ratio of *Z* to *E* isomers was calculated by fitting two Gaussian peaks to the UV–vis spectra according to their

simulated UV–vis spectra (Fig. S18) [30]. A 98% *E*-C*n* HAT content at the PSS_{410} was estimated from this fit (Table S1). In addition, the conversion efficiency of C*n* HAT in solution following irradiation was studied by ^{1}H NMR spectroscopy. All studied C*n* HATs showed similar photophysical properties, owing to the similarity of their electronic structures. Upon 410 nm light irradiation of the C*n* HAT a 98–99% content of the *E* isomer was found for PSS_{410} (Figs. S19-S22). The quantum yield ($\Phi_{Z\rightarrow E}$) of the process was determined to be 3.1–4.0% (Figs. S23, S25, S27, S29). The back isomerization can be triggered by irradiating the samples with 340 nm light. As shown in the blue curve of Fig. 1, irradiation of the samples with 340 nm light results in a redshift of λ_{max} to 364 nm with a PSS_{340} consisting of 77% *Z*-C*n* HAT (Gaussian fit, table S1), similar to that observed at the PSS_{340} of C6 HAT. These results demonstrate that the efficiency of the *Z*-to-*E* and the back isomerization is independent of the carbon chain length of the linker in the solution. Irradiation of the obtained samples with 340 nm light yields a PSS_{340} consisting of 77–78% of the *Z* isomer using ^{1}H NMR spectroscopy (Figs. S19-S22) with $\Phi_{E\rightarrow Z}$ of 5.6–8.3% (Figs. S24, S26, S28, S30). The half-life ($\tau_{1/2}$) of the *E* isomer was measured to be 196–370 years at 298 K using the model compounds Cn Br (Table S2).

3.3. Photoisomerization of Cn HAT (n = 3, 8, 10, 11) in the solid state

Confocal Raman spectroscopy was employed to investigate the photoisomerization of C*n* HAT powders. For getting information about the expected changes in the Raman spectra of C*n* HATs upon photoisomerization, density functional theory (DFT) calculations with the B3LYP method using a basis set of 6-31G [30] were performed to simulate the vibrational spectra of the *Z* and *E* isomers of C*n* HAT (Fig. S31). We found that all the Raman spectra of the *Z* and *E* isomers of C*n* HAT molecules show similar features. In the spectrum of *Z* isomers, the peaks at 990 and 1,618/cm correspond to the breathing and stretching modes of the benzene rings, respectively. Both peaks remain the same after *Z*-to-*E* isomerization. Upon the *Z*-to-*E* isomerization, the peaks at 1,436 and 1,475/cm, which are associated with the C=N stretching mode, shift to 1,565/cm. Additionally, the peak corresponding to the C=O stretching mode shifts from 1,670/cm to 1,737/cm, which is attributed to the disappearance of the intramolecular hydrogen bonding between the carbonyl oxygen of the ester and the nitrogen of the aniline. Moreover, the intensity of the peak at 1,024/cm (the C–H bending mode) increases, and the C–N stretching mode slightly shifts from 1,508/cm to 1,524/cm. The peaks at 1,576 and 1,737/cm are characteristic peaks of the *E* isomer, and the peaks at 1,435, 1,476, and 1,670/cm are the characteristic peaks of the *Z* isomer. It is noteworthy that because of the small Raman cross-section of the C=O bond, this vibrational mode is usually very weak in Raman spectra. Hence, the decrease of the peaks at 1,435 and 1,475/cm and the new peak appearing at 1,565/cm were used to determine the *Z*-to-*E* isomerization of the molecules.

The experimental Raman spectra of C*n* HAT powder samples before and after irradiation at 415 nm or 340 nm were collected and are shown in Fig. 2. Before light irradiation, all the Raman spectra (black curves in Fig. 2) of C*n* HAT powders show similar features and are in good agreement with the simulated spectrum of the *Z*

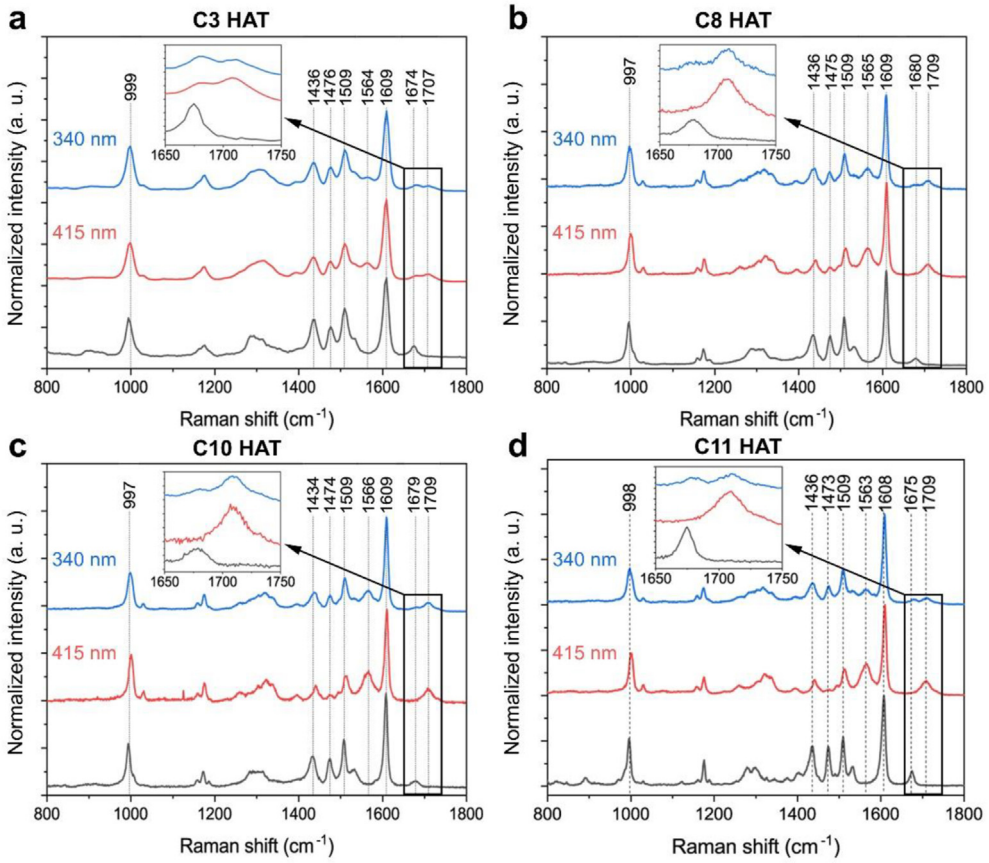

Fig. 2. Confocal Raman spectra of C*n* HAT (n = 3, 8, 10, 11) powders before (black curves) and after irradiation with 415 nm light (red curves), followed by irradiation with 340 nm light (blue curves), (**a**) C3 HAT; (**b**) C8 HAT; (**c**) C10 HAT; (**d**) C11 HAT. Insets: Zoomed-in spectra in the range between 1,650 and 1,750/cm of C*n* HAT powders before and after light irradiation.

isomer. After irradiation with 415 nm light, we observed similar changes in the Raman spectra in all cases, but to various extents for the different compounds. For C3 HAT (Fig. 2a), a slight decrease in intensity of the peaks at 1,436 and 1,476/cm and a new peak appearing at 1,565/cm were observed. Moreover, the peak intensity at 1,680/cm decreases while a new peak appears at 1,709/cm (red curve shown in the insets). All these changes are consistent with the results of the predicted Raman spectra, suggesting that some of the *Z*-C3 HAT molecules have isomerized to the *E* form. For C8 HAT, C10 HAT, and C11 HAT (Fig. 2b–d), the peak intensity at 1,436/cm significantly decreased and the peak at 1,475/cm almost disappears, while a prominent peak appears at 1,709/cm. Additionally, the peak at 1,680/cm completely shifts to 1,709/cm (the red curves shown in the insets). Such changes indicate a very high photoconversion efficiency. As described above, the peaks at 1,680 and 1,709/cm only refer to the C=O vibrational mode, and thus the ratio of these two peaks can be used to estimate the PSS. A Gaussian fit was performed to calculate the ratio of the two isomers (Fig. S32). For C3 HAT, the *E* and *Z* ratio at PSS_{415} is calculated to be 48:52, which is much smaller than that in the solution phase. For C8, C10, and C11 HAT, this ratio is 97:3, 92:8, and 97:3 (see Table S3), respectively. The switching efficiency of these compounds is comparable to our earlier results reported for C6 HAT powders. The lower conversion efficiency of C3 HAT powders upon 415 nm light irradiation is likely because of the strong intermolecular interactions of C3 HAT. The molecular volume of C3 HAT is smaller than that of other C*n* HAT (n = 8, 10, 11) molecules, and hence, we speculate that the hydrazone skeleton of C3 HAT is more closely packed in the bulk material [22], i.e., there is a lesser free volume for C3 HAT to accommodate the change in shape upon isomerization, and stronger steric effects among molecules, compared with other C*n* HAT molecules.

Next, we irradiated the samples with 340 nm light. As shown in the blue curves of Fig. 2, the intensities of the characteristic Raman bands for the *E* isomer at 1,564 and 1,709/cm decrease in all cases, while the intensities of the peaks at 1,436, 1,476, and 1,675/cm partially recover, which means that part of the *E* isomer has isomerized back to the *Z* state. The *E*/*Z* ratio at PSS_{340} for C*n* HAT (n = 3, 8, 10, 11) was calculated to be 39:61, 71:29, 75:25, and 59:41, respectively. The highest back conversion efficiency was observed in C11 HAT powder (38% of the *E*-C11 HAT have isomerized), which could be attributed to the loosest packing of C11 HAT compared with other C*n* HAT molecules. Notably, although the Z-to-E isomerization efficiency of C11 HAT powder after 410 nm light irradiation was comparable to that of C11 HAT in toluene, the back conversion efficiency is much lower than that of C11 HAT in toluene (75% of the *E*-C11 HAT has isomerized). This difference is tentatively ascribed to the different packing of the Z and E isomers of C11 HAT in powder samples. We speculate that after C11 HAT molecules switch from *Z* to *E*, the *E* molecules are more closely packed in bulk materials than the *Z* molecules due to the smaller molecular volume.

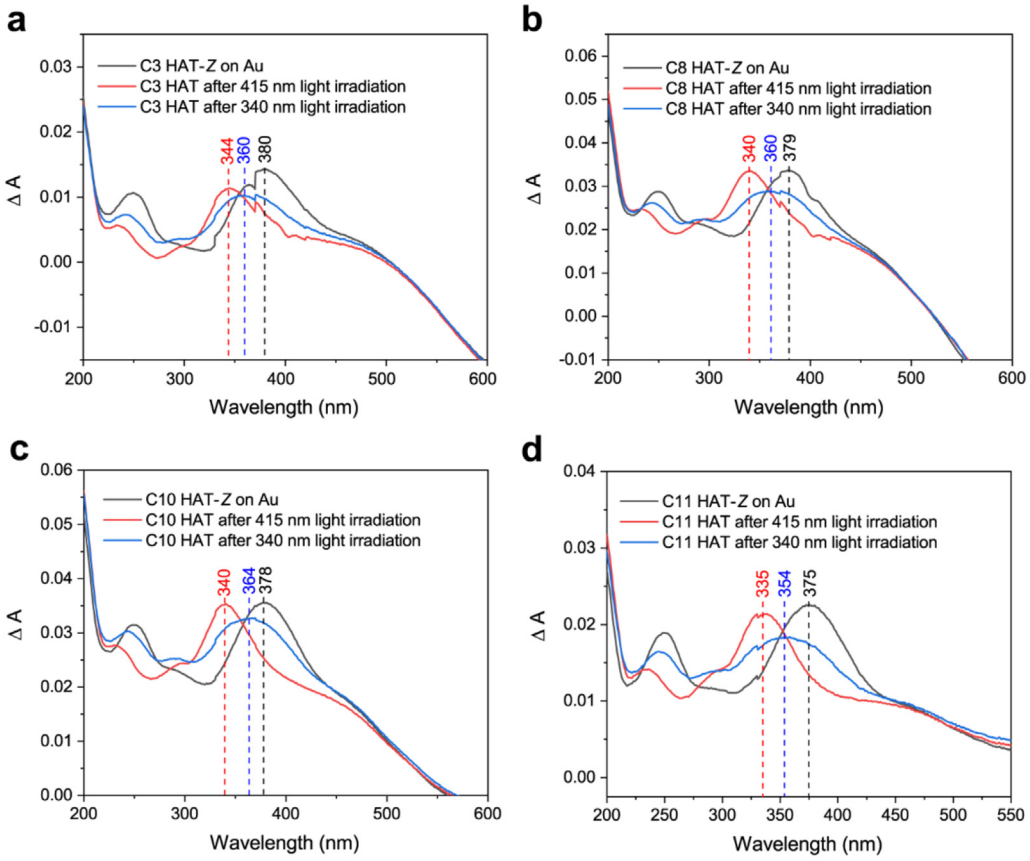

Fig. 3. UV–vis spectra of C*n* HAT (n = 3, 8, 10, 11) SAMs on Au before (black curve) and after irradiation with 415 nm light (red curve), followed by irradiation with 340 nm light (blue curve) (**a**). C3 HAT; (**b**). C8 HAT; (**c**). C10 HAT; (**d**). C11 HAT. The y-axis (Δ A) represents the absorbance of C*n* HAT SAMs; the absorbance of the Au substrate has been subtracted from the total absorbance of C*n* HAT SAMs on Au. The negative absorbance shown in the Figures is due to the imperfect subtraction of the absorbance of Au. The discrete steps at 370 and 420 nm are due to the change of grating.

3.4. Photoisomerization of a Cn HAT (n = 3, 8, 10, 11) monolayer on a metal surface

Of central interest in this work is the study of the alkyl chain length on the photoisomerization of HAT at the monolayer level. For investigating the switching behavior of hydrazone at the molecular level, C*n* HAT molecules were self-assembled on a metal surface to form monolayers. A common strategy to produce self-assembled monolayers (SAMs) is through adsorption of alkanethiols on Au, Ag, and other metals due to the high affinity of the thiolate headgroup for the metal substrate [51]. In our model molecules, alkanethiol linkers were attached to the hydrazone skeleton, and therefore, the assembly of C*n* HAT molecules on a metal surface could be more complicated than that of simple alkanethiols on metal. Due to the large terminal group (hydrazone skeleton), the resulting structures probably are more disordered and less dense than those formed from alkanethiols, but the coverage of C*n* HATs on Au is still expected to be close to a full monolayer. For quantifying the conversion efficiency of C*n* HAT SAMs on Au surfaces after light irradiation, UV−vis spectra of these samples were recorded and are shown in Fig. 3. Before any light irradiation, the maximum absorption peak in the UV spectra of the C*n* HAT SAMs appears between 375 and 380 nm for C3, C8, C10, and C11 HAT (Fig. 3, black curves). After irradiation at 415 nm, all the C*n* HAT SAMs samples exhibited a ca. 40 nm hypsochromic shift. As shown in Table 1, the *E*/*Z* ratio at PSS_{415} for C3 HAT was calculated to be 53:47 based on Gaussian fitting (Fig. S33), while the *E*/*Z* ratio at PSS_{415} for other HAT compounds was as high as 90:10 (Table 1). Compared with other HAT compounds, the C3 HAT SAM on Au thus exhibits a lower PSS after irradiation at 415 nm. A drop in conversion efficiency of C3 HAT could result from steric/packing effects, as explained above for the case of C3 HAT powder. To assess the contribution of steric effects, we investigated the isomerization of C3 HAT on Au diluted in a 10-fold excess of.

Propanethiol using UV−vis spectroscopy. As shown in Fig. S34, the *E*/*Z* ratio at PSS_{415} of the diluted C3 HAT SAM is also 53:47, indicating that lowering the packing density of C3 HAT on Au does not affect its conversion efficiency. Although the phase separation [52] of binary thiol compounds is likely to occur under ambient conditions, the steric effects in the diluted C3 HAT SAM is significantly reduced. This observation leads us to conclude that the low isomerization of C3 HAT results from strong quenching of the excited C3 HAT molecules by the Au surface. The isomerization of on-surface photoswitches concurrently involves several complex processes, such as direct molecular excitation and/or substrate-mediated charge transfer processes. First, upon irradiation at 415 nm, some of the molecules are promoted to an excited state. However, these excited adsorbates are prone to relax to the ground state *via* a non-radiative decay because of efficient electron/energy transfer to the metal surface. On the other hand, we have proposed a substrate-mediated charge transfer mechanism [30] for the isomerization of an on-surface hydrazone photoswitch, supported by our previous experimental results. According to this mechanism, the excitation of light first induces the formation of hot carriers in the d band of the metal surface, followed by transfer of these hot carriers to the molecules, leading to the formation of excited intermediates, which then results in isomerization. The whole process is also dependent on the distance between the switch group and the metal surface, as the tunneling rate of these hot carriers from the saturated alkyl chain to the switching group (the C=N bond) decays exponentially as a function of the donor-acceptor distance based on Marcus theory [53]. At the same time, the further away the hydrazone is from the surface, the more direct light isomerization will take place. The interplay between these effects results in an enhancement in the *E*/*Z* ratio at PSS_{415} as the linker length is increased from 1 nm to 2 nm. Ultimately, the outcome of these effects is that the *E*/*Z* ratio reaches a maximum value of 90:10 for C8 HAT and above, which is higher than that reported for C6 HAT (82:18). One can speculate that the latter is the sweet spot where the Marcus theory is mainly working.

Table 1
Photochemical properties of C*n* HAT (n = 3, 8, 10, 11) SAMs on Au.

Parameter	C3 HAT	C8 HAT	C10 HAT	C11 HAT
$\lambda_{max,\ Z\ isomer}$ (nm)	380	380	379	375
$\lambda_{max,\ PSS\ 415}$ (nm)	344	340	340	335
$([E]:[Z])_{PSS415}$ (%)	53:47	90:10	90:10	89:11
$\lambda_{max,\ PSS\ 340}$ (nm)	360	360	364	354
$([E]:[Z])_{PSS340}$ (%)	41:59	41:59	42:58	44:56

The samples were also irradiated at 340 nm, and the maximum absorption peak was found to shift back by a different extent, to between 354 nm and 364 nm (Fig. 3, blue curves), indicating that back isomerization occurs. Subsequently, Gaussian functions were again fitted to the absorption peaks (Fig. S35). Based on the area ratio of the two absorption peaks of both isomers, the percentage of the *E*-C*n* HAT molecules was calculated. Table 1 summarizes the absorption wavelength of each sample and the conversion efficiency in %. Surprisingly, unlike the back isomerization of C*n* HAT in the solid state (Table S3), which varies dramatically as a function of

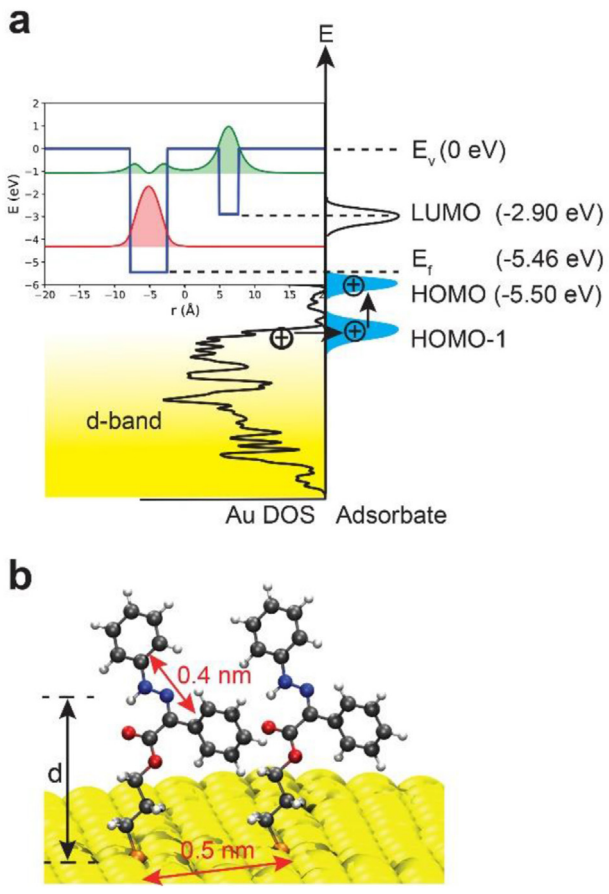

Fig. 4. (**a**). Diagram of the energy levels of C3 HAT on Au (111) aligned with the projected density of states (DOS) of optimized structures. Upper part: solution of the one-dimensional double-well model for C3 HAT. The red line represents the electron distribution of the ground state, and the green line represents that of the excited state. (**b**). Atomic model illustrating how C3 HAT molecules are adsorbed on Au (111) (not to scale).

the linker length, C*n* HAT SAMs on Au reached a PSS_{340} of around 41% *E*-C*n* HAT in all cases. When comparing the *E*/*Z* isomer ratio following irradiation at 415 nm (forward reaction) with that for irradiation at 340 nm (back reaction), it becomes evident that back isomerization for C3 HAT is also less efficient than for the other C*n* HAT molecules. For verifying this, C*n* HAT compounds were dissolved in EtOH followed by irradiation with 415 nm light, which resulted in a PSS_{415} of 93% *E*-C*n* HAT (Fig. S36). Subsequently, the Au substrates were immersed in these solutions to obtain *E*-C*n* HAT SAMs on Au. Irradiation of these samples with 340 nm light results in various *E*/*Z* ratios at PSS (Fig. S37). The *E* isomer ratio at PSS_{340} for C3 HAT is only 51%, and it decreases to 35% for C8 HAT and further decreases to 25% for C10 HAT and C11 HAT. These results confirm that the back isomerization is also prone to quenching by the metal surface when the alkyl chain length is short. The surface quenching effect on the back isomerization is almost negligible for C10 HAT and C11 HAT, which might be an indication of direct light isomerization. Notably, the back isomerization for all C*n* HAT is higher than that through direct switching on Au (shown in Table 1). We speculate that the discrepancy between two experiments may be due to the different topography of Au substrates prepared in two batches, which resulted in different molecular orientations and packing density of C*n* HAT adsorbed on Au. These factors inevitably affected the conversion efficiency.

To shed light on the surface quenching effect on the isomerization reaction, we carried out DFT calculations for C*n* HAT molecules adsorbed on Au(111) surfaces. Based on these results, we propose a one-dimensional double-well model to understand the observed phenomenon. As shown in Fig. 4a, square potentials are used in a double-well model, whose depths are given by the work function (E_f - E_v) of the metal and electron affinity (E_{LUMO} - E_v) of the C*n* HAT molecules. The double-well is separated by the length of the alkyl chain linker. We approximate the width of the potentials to be $W_{metal} = 5.2$ and $W_{mol} = 2.8$ Å, which are taken from the average distance between molecules on an Au surface ($\sqrt{3}$ a, being the average bond length of Au–Au) and the length of the dihedral atoms (C–C=N–N, corresponding to the LUMO orbitals), as shown in Fig. 4b. We solved this double-well problem using the Schrödinger equation to approximate the energy level of the ground (red) and excited states (green). As suggested by the double-well model, with increasing the length of the linker, excitation energy decreases and levels out at n = 8. When the linker is short (n = 3), the excitation energy is 3.10 eV, which is slightly higher than that of the HAT molecules with a longer linker ($E_{ex} = 3.02$ eV), suggesting a shorter lifetime of the excited state of C3 HAT (see details about the calculations in supporting information). As shown in Fig. 4a, photo-induced hot carriers in the excited states of C3 HAT are partially trapped in the potential well of Au, and therefore, excited molecules are easily quenched by the Au surface, in contrast to other HAT molecules with a longer linker (Fig. S38 and Table S4). This is in good agreement with our experimental results. Moreover, the excitation energy of C*n* HAT on Ag was calculated. We found a similar trend as that observed for C*n* HAT on Au (see Fig. S39 and Table S5), which means that the isomerization of C3 HAT on Ag is probably quenched by the surface.

The UV spectroscopic results show that C8 HAT on Au exhibits the highest photoconversion after irradiation at 415 nm. When we further increase the linker length, it does not lead to an even higher conversion. As a cross validation, the photoisomerization of a C8 HAT SAM on Au was verified by TERS. TER spectra of a C8 HAT SAM on Au before and after irradiation at 415 nm are shown in Fig. 5a,c, respectively. In the TER spectrum of a C8 HAT SAM, we observed

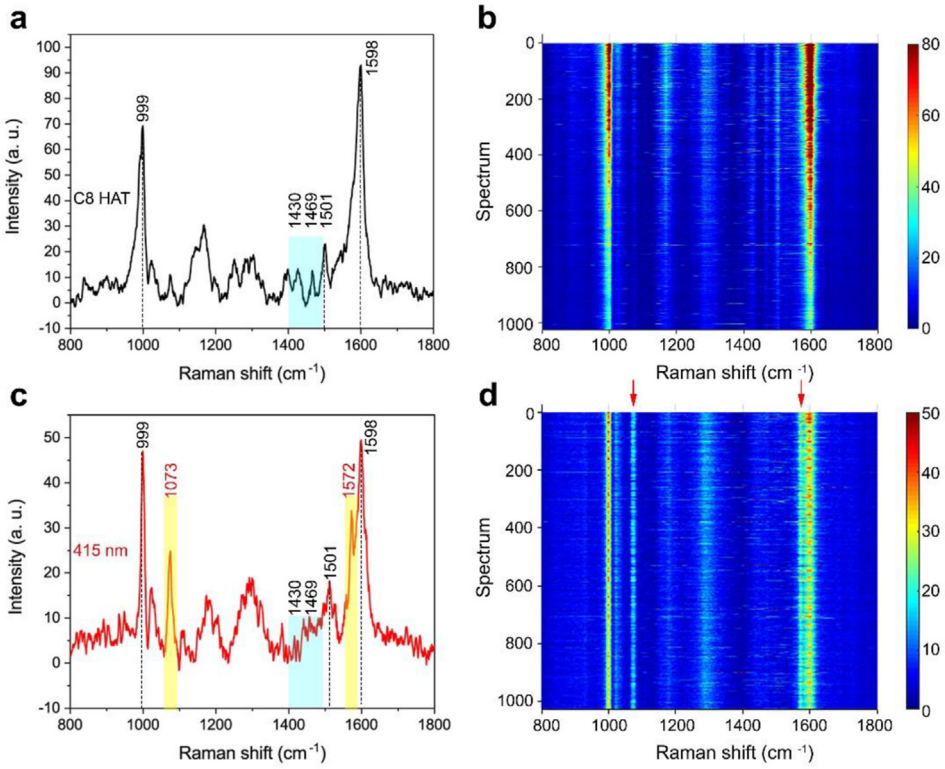

Fig. 5. (**a,c**) Baseline corrected TER spectrum of a C8 HAT SAM on Au surface before (**a**, black curve) and after irradiation with 415 nm light (**b**, red curve). The peaks at 1,430 and 1,469 cm^{-1} marked with a blue rectangle correspond to the *Z* isomer. The peaks at 1,073 and 1,572 cm^{-1} marked with yellow rectangles correspond to the *E* isomer. (**b, d**) Waterfall plot of all TER spectra from maps of a C8 HAT SAM on Au before (**b**) and after irradiation with 415 nm light (**d**). The red arrows label the position of the peaks at 1,073 cm^{-1} and 1,573 cm^{-1}. The size of all maps is 1 × 1 μm^2 with a 31 nm pixel size. All TER spectra were normalized to the Raman peak at 1,598 cm^{-1}.

similar spectral features as we found in the confocal Raman spectra, consistent with the predicted Raman spectrum of the *Z* isomer, except for the disappearance of the peak at 1,680/cm. This could result from the low signal-to-noise ratio of the spectrum, as the intensity of this peak is intrinsically weak and further reduced because of the surface selection rule of TERS [30], in which in-plane vibrations are canceled by the induced mirror dipoles in the substrate. After irradiation at 415 nm, the peaks at 1,430 and 1,469/cm almost disappear, while the intensity of the peak at 1,073/cm significantly grows, and simultaneously a new peak appears at 1,572/cm. All these spectral differences indicate the occurrence of the *Z*-to-*E* isomerization. Furthermore, to quantify the isomerization ratio of C8 HAT after 415 nm light irradiation, we collected TERS maps of a C8 HAT SAM on Au before and after irradiation at 415 nm with a pixel size of ca. 30 nm. As shown in Fig. 5b,d, after irradiation with 415 nm light, we observed the same spectral changes in most of the TER spectra within the map as those observed in the single TER spectrum. This indicates that most of the *Z*-C8 HAT molecules have isomerized to the *E* form. As mentioned above, the peak at 1,572/cm is characteristic of the *E* isomer, and thus, we could use this peak to calculate the conversion efficiency. As shown in the TERS map of the peak intensity at 1,572/cm (Fig. S39), this peak appears in 85% of the spectra. This value agrees with the conversion efficiency calculated from the UV−vis spectroscopic results of the C8 HAT SAM on Au. Apart from C8 HAT, we also collected TERS maps of C3 HAT/C11 HAT before and after irradiation at 415 nm (Figs. S40 and S41). In both cases, we observed spectral features similar to those found in the TERS maps of C8 HAT, indicating the occurrence of isomerization upon light irradiation. Furthermore, all TER spectra within a map were accumulated and averaged to obtain statistical information. Notably, we found that a small peak appears at 1,709/cm in the averaged TER spectra of C3 and C11 HAT SAMs on Au after irradiation at 415 nm, while the intensity of the peak at 1,680/cm decreases (Figs. S40c and S41c). All these spectra changes confirm the isomerization.

According to our previous experimental results of C6 HAT, isomerization of C6 HAT on Ag cannot be triggered by irradiation with 415 nm photons but only by irradiation at 280 nm. We, therefore, sought to verify, using UV−vis spectroscopy, whether C*n* HAT SAMs on Ag can undergo *Z*-to-*E* isomerization with irradiation at 415 nm or 280 nm. The experimental results are shown in Fig. S42. In contrast to the C*n* HAT SAMs on Au, no significant shift of the maximum absorption wavelength in the absorption spectra of C*n* HAT SAMs on Ag was observed, which demonstrates the absence of photoisomerization. Based on the substrate-mediated isomerization mechanism proposed, a light source with an energy of at least higher than 3.9 eV is needed to trigger the isomerization of HAT on Ag. We, therefore, irradiated the samples with a wavelength of 280 nm (E = 4.4 eV, Fig. S43). In the absorption spectra of C8, C10, and C11 HAT SAMs.

On Ag after irradiation at 280 nm, we found a significant blue shift in the absorption peak, which indicates that most of the molecules have isomerized to the *E* form. Interestingly, in the cases of C3 HAT, we did not observe such a peak shift, which could be tentatively attributed to the strong inhibition of the excited molecule by the Ag. Overall, these results support the proposed substrate-mediated isomerization mechanism.

4. Conclusions

In summary, we have synthesized a series of bistable hydrazone switches containing alkyl thiolate linkers (C*n* HAT, n = 3, 8, 10, and 11) of various lengths, ranging from around 1 to 2 nm. The length effect of carbon chain linker on the photoisomerization of the hydrazone switches was systematically investigated in solution, in the solid state, and as a monolayer assembled on metal surfaces, using UV−vis spectroscopy, confocal Raman spectroscopy, and TERS. In solution, the conversion efficiency of C*n* HATs upon irradiation at 415 nm or 340 nm was found to be independent of carbon chain length. We also monitored the conversion efficiency of C*n* HAT SAMs on Au and Ag using UV−vis spectroscopy and TERS. Interestingly, we found that the *Z*-to-*E* conversion efficiency of C*n* HAT SAMs on Au at PSS_{415} increases as a function of the alkyl chain length and saturates after the carbon number of the alkyl chain reaches 8. A similar trend was found for the back isomerization. These results reflect the synergy between the metal surface-induced quenching and the previously proposed substrate-mediated photoisomerization mechanism. When the length of the carbon chain increases, quenching by the surface strongly decreases, as confirmed by DFT calculations. On the other hand, the proposed photoisomerization mechanism would stop working at a certain distance since the electron transfer rate decays exponentially with donor−acceptor distance. Subsequently, direct light isomerization starts playing a larger role. C*n* HAT SAMs, similar to C6 HAT, were found not to isomerize on Ag surfaces upon irradiation at 415 nm but can isomerize upon irradiation at 280 nm, except for C3 HAT. Overall, these results confirm the previously proposed isomerization mechanism. Our study suggests that the isomerization of HAT monolayers assembled on metal surfaces is not only affected by the linker length but also by the substrates. To increase the isomerization efficiency of photoswitches on surfaces, a rational design of their chemical structure and an appropriate choice of the substrate are of great importance. This understanding contributes to developing effective photocontrollable surfaces using molecular switches.

Author contributions

R. Z. and I. A. supervised the project. L.-Q. Z. conceived of the ideas. L.-Q. Z. and S. Y. designed the experiments. S. Y. synthesized molecules and performed the characterization of the compounds. L.-Q. Z. and S. K. performed the experiments. V. V. R. and J. L. performed the DFT calculations. L.-Q. Z. and S. Y. wrote the manuscript with the help of J. L. All authors discussed the results and commented on the manuscript.

Notes

The original data used in this publication are made available in a curated data archive at ETH Zurich (https://www.research-collection.ethz.ch) under the https://doi.org/10.3929/ethz-b-000493421.

Declaration of competing interest

The authors declare the following financial interests/personal relationships which may be considered as potential competing interests: The authors have no financial conflicts to declare, however one of the authors, Ivan Aprahamian of Dartmouth college, is a co-guest editor for the special issue of Materials Today Chemistry for “Fraser’s 80th birthday”.

Acknowledgments

L.-Q. Z. thanks the Chinese Scholarship Council for financial support (scholarship # 201506190126). We thank the High-Performance Computing Team at ETH Zurich for help with DFT calculations, and the ERC program (grant # 741431−2DNanoSpec) for financial support. I.A. is grateful to the NSF (CHE-1807428) for the generous support.

Appendix A. Supplementary data

Supplementary data to this article can be found online at https://doi.org/10.1016/j.mtchem.2022.100797.

References

[1] B. Feringa, N. Koumura, R. Van Delden, M. Ter Wiel, Light-driven molecular switches and motors, Appl. Phys. A 75 (2002) 301–308, https://doi.org/10.1007/s003390201338.

[2] M. Natali, S. Giordani, Molecular switches as photocontrollable "smart" receptors, Chem. Soc. Rev. 41 (2012) 4010–4029, https://doi.org/10.1039/C2CS35015G.

[3] B.L. Feringa, W.R. Browne, Molecular Switches, 2 Volume Set, John Wiley & Sons, 2011.

[4] W.-L. Chiang, T.-T. Lin, R. Sureshbabu, W.-T. Chia, H.-C. Hsiao, H.-Y. Liu, C.-M. Yang, H.-W. Sung, A rapid drug release system with a NIR light-activated molecular switch for dual-modality photothermal/antibiotic treatments of subcutaneous abscesses, J. Contr. Release 199 (2015) 53–62, https://doi.org/10.1016/j.jconrel.2014.12.011.

[5] S.M. Dirk, D.W. Price Jr., S. Chanteau, D.V. Kosynkin, J.M. Tour, Accoutrements of a molecular computer: switches, memory components and alligator clips, Tetrahedron 57 (2001) 5109–5121, https://doi.org/10.1016/S0040-4020(01)00361-1.

[6] Z. Liu, H.I. Wang, A. Narita, Q. Chen, Z. Mics, D. Turchinovich, M. Klaui, M. Bonn, K. Mullen, Photoswitchable micro-supercapacitor based on a diarylethene-graphene composite film, J. Am. Chem. Soc. 139 (2017) 9443–9446, https://doi.org/10.1021/jacs.7b04491.

[7] P. Dandawate, E. Khan, S. Padhye, H. Gaba, S. Sinha, J. Deshpande, K.V. Swamy, M. Khetmalas, A. Ahmad, F.H. Sarkar, Synthesis, characterization, molecular docking and cytotoxic activity of novel plumbagin hydrazones against breast cancer cells, Bioorg. Med. Chem. Lett. 22 (2012) 3104–3108, https://doi.org/10.1016/j.bmcl.2012.03.060.

[8] Y. Hirshberg, Reversible formation and eradication of colors by irradiation at low temperatures. A photochemical memory model, J. Am. Chem. Soc. 78 (1956) 2304–2312.

[9] W. Luo, Y. Feng, C. Cao, M. Li, E. Liu, S. Li, C. Qin, W. Hu, W. Feng, A high energy density azobenzene/graphene hybrid: a nano-templated platform for solar thermal storage, J. Mater. Chem. A 3 (2015) 11787–11795, https://doi.org/10.1039/C5TA01263E.

[10] X. Guo, B. Shao, S. Zhou, I. Aprahamian, Z. Chen, Visualizing intracellular particles and precise control of drug release using an emissive hydrazone photochrome, Chem. Sci. 11 (2020) 3016–3021, https://doi.org/10.1039/C9SC05321B.

[11] X. Su, I. Aprahamian, Hydrazone-based switches, metallo-assemblies and sensors, Chem. Soc. Rev. 43 (2014) 1963–1981, https://doi.org/10.1039/C3CS60385G.

[12] H. Abou-Yousef, T.A. Khattab, Y.A. Youssef, N. Al-Balakocy, S. Kamel, Novel cellulose-based halochromic test strips for naked-eye detection of alkaline vapors and analytes, Talanta 170 (2017) 137–145, https://doi.org/10.1016/j.talanta.2017.04.002.

[13] V. Blanco, D.A. Leigh, V. Marcos, Artificial switchable catalysts, Chem. Soc. Rev. 44 (2015) 5341–5370, https://doi.org/10.1039/C5CS00096C.

[14] Q. Qiu, Y. Shi, G.G. Han, Solar energy conversion and storage by photoswitchable organic materials in solution, liquid, solid, and changing phases, J. Mater. Chem. C (2021), https://doi.org/10.1039/D1TC01472B.

[15] H.D. Bandara, S.C. Burdette, Photoisomerization in different classes of azobenzene, Chem. Soc. Rev. 41 (2012) 1809–1825.

[16] M. Irie, T. Fukaminato, K. Matsuda, S. Kobatake, Photochromism of diarylethene molecules and crystals: memories, switches, and actuators, Chem. Rev. 114 (2014) 12174–12277, https://doi.org/10.1039/C1CS15179G.

[17] R. Klajn, Spiropyran-based dynamic materials, Chem. Soc. Rev. 43 (2014) 148–184, https://doi.org/10.1039/C3CS60181A.

[18] B. Shao, I. Aprahamian, Hydrazones as new molecular tools, Inside Chem. 6 (2020) 2162–2173, https://doi.org/10.1016/j.chempr.2020.08.007.

[19] Q. Li, H. Qian, B. Shao, R.P. Hughes, I. Aprahamian, Building strain with large macrocycles and using it to tune the thermal half-lives of hydrazone photochromes, J. Am. Chem. Soc. 140 (2018) 11829–11835, https://doi.org/10.1021/jacs.8b07612.

[20] B. Mravec, A. Marini, M. Tommasini, J. Filo, M. Cigáň, M. Mantero, S. Tosi, M. Canepa, A. Bianco, Structural and spectroscopic properties of benzoylpyridin-based hydrazones, ChemPhysChem (2021), https://doi.org/10.1002/cphc.202000941.

[21] A. Ryabchun, Q. Li, F. Lancia, I. Aprahamian, N. Katsonis, Shape-persistent actuators from hydrazone photoswitches, J. Am. Chem. Soc. 141 (2019) 1196–1200, https://doi.org/10.1021/jacs.8b11558.

[22] B. Shao, H. Qian, Q. Li, I. Aprahamian, Structure property analysis of the solution and solid-state properties of bistable photochromic hydrazones, J. Am. Chem. Soc. 141 (2019) 8364–8371, https://doi.org/10.1021/jacs.9b03932.

[23] N. Tallarida, L. Rios, V.A. Apkarian, J. Lee, Isomerization of one molecule observed through tip-enhanced Raman spectroscopy, Nano Lett. 15 (2015) 6386–6394, https://doi.org/10.1021/acs.nanolett.5b01543.

[24] C. Yun, A. Javier, T. Jennings, M. Fisher, S. Hira, S. Peterson, B. Hopkins, N. Reich, G. Strouse, Nanometal surface energy transfer in optical rulers, breaking the FRET barrier, J. Am. Chem. Soc. 127 (2005) 3115–3119, https://doi.org/10.1021/ja043940i.

[25] R. Bilewicz, M. Majda, Formation of passivating monolayers and incorporation of electroactive reagents, Langmuir 7 (1991) 2794–2802, https://doi.org/10.1021/la00059a063.

[26] M. Alemani, S. Selvanathan, F. Ample, M.V. Peters, K.-H. Rieder, F. Moresco, C. Joachim, S. Hecht, L. Grill, Adsorption and switching properties of azobenzene derivatives on different noble metal surfaces: Au (111), Cu (111), and Au (100), J. Phys. Chem. C 112 (2008) 10509–10514, https://doi.org/10.1021/jp711134p.

[27] S. Fatayer, F. Albrecht, Y. Zhang, D. Urbonas, D. Peña, N. Moll, L. Gross, Molecular structure elucidation with charge-state control, Science 365 (2019) 142–145, https://doi.org/10.1126/science.aax5895.

[28] G. Pace, V. Ferri, C. Grave, M. Elbing, C. von Hänisch, M. Zharnikov, M. Mayor, M.A. Rampi, P. Samorì, Cooperative light-induced molecular movements of highly ordered azobenzene self-assembled monolayers, Proc. Natl. Acad. Sci. Unit. States Am. 104 (2007) 9937–9942, https://doi.org/10.1073/pnas.0703748104.

[29] L.-Q. Zheng, X. Wang, F. Shao, M. Hegner, R. Zenobi, Nanoscale chemical imaging of reversible photoisomerization of an azobenzene-thiol self-assembled monolayer by tip-enhanced Raman spectroscopy, Angew. Chem. Int. Ed. 57 (2018) 1025–1029, https://doi.org/10.1002/ange.201710443.

[30] L.-Q. Zheng, S. Yang, J. Lan, L. Gyr, G. Goubert, H. Qian, I. Aprahamian, R. Zenobi, Solution phase and surface photoisomerization of a hydrazone switch with a long thermal half-life, J. Am. Chem. Soc. 141 (2019) 17637–17645, https://doi.org/10.1021/jacs.9b07057.

[31] M.S. Anderson, Locally enhanced Raman spectroscopy with an atomic force microscope, Appl. Phys. Lett. 76 (2000) 3130–3132, https://doi.org/10.1063/1.126546.

[32] N. Hayazawa, Y. Inouye, Z. Sekkat, S. Kawata, Metallized tip amplification of near-field Raman scattering, Opt Commun. 183 (2000) 333–336, https://doi.org/10.1016/S0030-4018(00)00894-4.

[33] R.M. Stockle, Y.D. Suh, V. Deckert, R. Zenobi, Nanoscale chemical analysis by tip-enhanced Raman spectroscopy, Chem. Phys. Lett. 318 (2000) 131–136, https://doi.org/10.1016/S0009-2614(99)01451-7.

[34] X. Wang, S.C. Huang, T.X. Huang, H.S. Su, J.H. Zhong, Z.C. Zeng, M.H. Li, B. Ren, Tip-enhanced Raman spectroscopy for surfaces and interfaces, Chem. Soc. Rev. 46 (2017) 4020–4041, https://doi.org/10.1039/C7CS00206H.

[35] J.H. Zhong, X. Jin, L.Y. Meng, X. Wang, H.S. Su, Z.L. Yang, C.T. Williams, B. Ren, Probing the electronic and catalytic properties of a bimetallic surface with 3 nm resolution, Nat. Nanotechnol. 12 (2017) 132–136, https://doi.org/10.1038/nnano.2016.241.

[36] T. Schmid, L. Opilik, C. Blum, R. Zenobi, Nanoscale chemical imaging using tip-enhanced Raman spectroscopy: a critical review, Angew. Chem. Int. Ed. 52 (2013) 5940–5954, https://doi.org/10.1002/anie.201203849.

[37] R. Zhang, Y. Zhang, Z. Dong, S. Jiang, C. Zhang, L. Chen, L. Zhang, Y. Liao, J. Aizpurua, Y. Luo, J.L. Yang, J.G. Hou, Chemical mapping of a single molecule by plasmon-enhanced Raman scattering, Nature 498 (2013) 82–86, https://doi.org/10.1038/nature12151.

[38] J. Lee, K.T. Crampton, N. Tallarida, V.A. Apkarian, Visualizing vibrational normal modes of a single molecule with atomically confined light, Nature 568 (2019) 78–82, https://doi.org/10.1038/s41586-019-1059-9.

[39] J. Xu, X. Zhu, S. Tan, Y. Zhang, B. Li, Y. Tian, H. Shan, X. Cui, A. Zhao, Z. Dong, J. Yang, Y. Luo, B. Wang, J.G. Hou, Determining structural and chemical heterogeneities of surface species at the single-bond limit, Science 371 (2021) 818–822, https://doi.org/10.1126/science.abd1827.

[40] E.A. Weiss, G.K. Kaufman, J.K. Kriebel, Z. Li, R. Schalek, G.M. Whitesides, Si/SiO2-Templated formation of ultraflat metal surfaces on glass, polymer, and solder supports: their use as substrates for self-assembled monolayers, Langmuir 23 (2007) 9686–9694, https://doi.org/10.1021/la701919r.

[41] J. Stadler, T. Schmid, R. Zenobi, Nanoscale chemical imaging using top-illumination tip-enhanced Raman spectroscopy, Nano Lett. 10 (2010) 4514–4520, https://doi.org/10.1021/nl102423m.

[42] J. Hutter, M. Iannuzzi, F. Schiffmann, J. VandeVondele, cp2k: atomistic simulations of condensed matter systems, Wiley Interdiscip. Rev. Comput. Mol. Sci. 4 (2014) 15–25, https://doi.org/10.1002/wcms.1159.

[43] T.D. Kühne, M. Iannuzzi, M.D. Ben, V.V. Rybkin, P. Seewald, F. Stein, T. Laino, R.Z. Khaliullin, O. Schütt, F. Schiffmann, CP2K: an electronic structure and molecular dynamics software package-Quickstep: efficient and accurate electronic structure calculations, J. Chem. Phys. 152 (2020) 194103, https://doi.org/10.1063/5.0007045.

[44] J.P. Perdew, K. Burke, M. Ernzerhof, Generalized gradient approximation made simple, Phys. Rev. Lett. 77 (1996) 3865, https://doi.org/10.1103/PhysRevLett.77.3865.

[45] S. Grimme, Semiempirical GGA-type density functional constructed with a long-range dispersion correction, J. Comput. Chem. 27 (2006) 1787–1799, https://doi.org/10.1002/jcc.20495.

[46] J. VandeVondele, J. Hutter, Gaussian basis sets for accurate calculations on molecular systems in gas and condensed phases, J. Chem. Phys. 127 (2007) 114105, https://doi.org/10.1063/1.2770708.

[47] J. VandeVondele, M. Krack, F. Mohamed, M. Parrinello, T. Chassaing, J. Hutter, Quickstep: fast and accurate density functional calculations using a mixed Gaussian and plane waves approach, Comput. Phys. Commun. 167 (2005) 103–128, https://doi.org/10.1016/j.cpc.2004.12.014.

[48] S. Goedecker, M. Teter, J. Hutter, Separable dual-space Gaussian pseudopotentials, Phys. Rev. B 54 (1996) 1703, https://doi.org/10.1103/PhysRevB.54.1703.
[49] C. Hartwigsen, S. Goedecker, J. Hutter, Relativistic separable dual-space Gaussian pseudopotentials from H to Rn, Phys. Rev. B 58 (1998) 3641, https://doi.org/10.1103/PhysRevB.58.3641.
[50] H. Qian, S. Pramanik, I. Aprahamian, Photochromic hydrazone switches with extremely long thermal half-lives, J. Am. Chem. Soc. 139 (2017) 9140–9143, https://doi.org/10.1021/jacs.7b04993.
[51] J.C. Love, L.A. Estroff, J.K. Kriebel, R.G. Nuzzo, G.M. Whitesides, Self-assembled monolayers of thiolates on metals as a form of nanotechnology, Chem. Rev. 105 (2005) 1103–1169, https://doi.org/10.1021/cr0300789.
[52] R. Klajn, Immobilized azobenzenes for the construction of photoresponsive materials, Pure Appl. Chem. 82 (2010) 2247–2279, https://doi.org/10.1351/PAC-CON-10-09-04.
[53] Y. Kim, A.J. Wilson, P.K. Jain, The nature of plasmonically assisted hot-electron transfer in a donor–bridge–acceptor complex, ACS Catal. 7 (2017) 4360–4365, https://doi.org/10.1021/acscatal.7b01318.